Energetics of Deep Alpine Valleys in Pooling and Draining Configurations

GABRIELE ARDUINI

Centre for Atmospheric and Instrumentation Research, University of Hertfordshire, Hatfield, United Kingdom, and Université Grenoble Alpes, CNRS, LEGI, Grenoble, France

CHARLES CHEMEL

National Centre for Atmospheric Science, and Centre for Atmospheric and Instrumentation Research, University of Hertfordshire, Hatfield, United Kingdom

CHANTAL STAQUET

Université Grenoble Alpes, CNRS, LEGI, Grenoble, France

(Manuscript received 4 May 2016, in final form 27 December 2016)

ABSTRACT

The Weather Research and Forecasting Model is used to investigate the nocturnal atmospheric boundary layer in a valley that opens either on a wider valley (draining configuration) or on a narrower valley (pooling configuration). One draining case and three weak to strong pooling cases are considered. Results show that the structure of the nocturnal boundary layer is substantially different for the draining and pooling configurations. Greater pooling corresponds with a deeper and colder boundary layer. Down-valley winds are weaker for pooling and draining configurations than in an equivalent valley opening directly on a plain. For the strong pooling case, an up-valley flow develops from the narrower to the wider valley during the evening transition, affecting the mass budget of the wider valley during that period. Considering the heat budget of the valley system, the contribution of the diabatic processes, when appropriately weighted, hardly varies along the valley axis. Conversely, the contribution of advection varies along the valley axis: it decreases for a pooling configuration and increases for a draining configuration. Consequently, for a pooling configuration, the heat transfer between the valley and the plain is reduced, thereby increasing the temperature difference between them. For the strong pooling case, this temperature difference can be explained by the valley-volume effect once the down-valley flow has developed. This occurs in a valley when the "extra" heat loss within the valley due to the surface sensible heat flux balances the heat input due to advection.

1. Introduction

The characteristics of the boundary layer in complex terrain are often tightly coupled with the variations of the underlying orography. The valley-to-plain temperature differences are primarily explained by the valley-volume effect, which can be quantified by the topographic amplification factor (TAF), a purely geometrical factor characterizing the reduction in the air volume within a valley compared to the equivalent volume if the terrain were flat (Wagner 1938; Vergeiner and Dreiseitl 1987; Muller and Whiteman 1988; Sakiyama 1990). McKee and O'Neal (1989) considered the intravalley variations of the TAF, thereby characterizing temperature gradients along the valley axis. In valleys characterized by a decreasing TAF (i.e., the valley widens) in the down-valley direction, the along-valley variation of the valley geometry induces a horizontal temperature gradient that promotes the development of a down-valley flow. Such valleys are defined as "draining" valleys. Conversely, when the TAF increases (i.e., the valley narrows) in the down-valley direction, the horizontal temperature gradient changes sign, hindering the development of a down-valley flow

Denotes content that is immediately available upon publication as open access.

Corresponding author: Gabriele Arduini, g.arduini@herts.ac.uk

DOI: 10.1175/JAS-D-16-0139.1

and promoting stagnation of the air in the valley. Such valleys are defined as ''pooling'' valleys. This classification was used by Lundquist et al. (2008) in the development of an algorithm to map mountainous regions sensitive to cold-air-pooling processes.

The use of the TAF to characterize along-valley variations in temperature holds when diabatic effects only are considered. When the valley atmosphere is decoupled from the free atmosphere above this is equivalent to neglecting the contribution of advection by thermally driven flows (along-slope and along-valley flows) to the valley heat (energy) budget, so that the temperature variations are due to radiative, sensible, and latent heat flux divergences only. The role of the thermally driven flows on the volume-averaged (bulk) valley heat budget has been debated in several modeling studies, most of them focusing on daytime conditions. Rampanelli et al. (2004) studied an idealized valley–plain configuration, highlighting the importance of the valley-scale circulation induced by thermally driven flows in the warming of the valley atmosphere during daytime. Schmidli and Rotunno (2010) studied a valley–plain configuration similar to that of Rampanelli et al. (2004), using a diagnostic framework providing the means to disentangle the valley-volume effect from the processes controlling the valley heat budget. The authors concluded that, despite the importance of the valley-scale circulation, the valley–plain temperature difference can be qualitatively explained by the valley-volume effect. Further work on the respective roles of the valley-scale circulation and the volume effect on the warming of the valley atmosphere during daytime was performed by Schmidli (2013), who considered an idealized set of two-dimensional and three-dimensional valleys. The author demonstrated that the net effect of the valley-scale circulation, when integrated over the scale of the valley, is to cool the valley atmosphere. Hence, the valley-volume effect is the main cause of the enhanced warming of a valley with respect to an adjacent plain region during daytime.

The effects of the along-slope (i.e., upslope or downslope) flows on the thermal structure of the valley atmosphere were studied by Catalano and Cenedese (2010) for a set of two-dimensional idealized valleys characterized by different volumes. Numerical simulations for a diurnal cycle indicated that the volume of the valley is a parameter key to controlling the growth of the nocturnal valley boundary layer (VBL), which, in turn, affects the evolution of downslope flows. Kiefer and Zhong (2011) investigated the impact of downslope flows on the atmospheric static stability of the nocturnal VBL of shallow, idealized valleys of varying widths. The authors found that the valley-averaged cooling rate is reduced in wider valleys because of the reduced impact of downslope flows on the valley heat budget. Similar conclusions were drawn by Katurji and Zhong (2012) in a more systematic sensitivity study, exploring a larger set of the parameter space. While most of these studies considered the effects of thermally driven flows on the structure of the VBL, the interplay between the two has received less attention. Burns and Chemel (2015) explored the two-way interactions taking place between downslope flows and the thermal structure of the nocturnal VBL in a two-dimensional idealized deep valley. Numerical model results indicated that the deepening of the nocturnal VBL above the ground-based inversion leads to a deceleration of downslope flows with time because of the reduction of the near-slope horizontal buoyancy deficit that ultimately drives downslope flows. Their work was extended by Arduini et al. (2016) by considering the interactions between the nocturnal valley-wind system (i.e., downslope and down-valley flows) and the thermal structure of the nocturnal VBL. The formation of down-valley flows was found to reduce the growth of the VBL, leading to downslope flows reaching a quasi-steady state. An analysis of the heat and mass budgets indicated that the air evacuating the VBL as a result of the down-valley flow is replenished by the advection of warmer air from downslope flows, with a small contribution from subsidence of air above the valley center.

Quantifying the effect of the thermally driven flows on the mass transport in and out of the valley atmosphere is key to understanding the atmospheric circulation at all scales (Rotach et al. 2014). The impact of the valley geometry on the structure of the VBL and its evolution was studied by Wagner et al. (2015a) for daytime conditions, for a set of idealized valley–plain systems. The authors showed that the valley-scale circulation is more sensitive to the valley width and depth than the valley length. The same conclusion holds for the associated mass transport processes. Wagner et al. (2015b) investigated more systematically the effect of along-valley orographic variations on transport processes during daytime. For a set of idealized valleys, the authors showed that a gradual narrowing of the valley cross section along the valley axis leads to an increase of the vertical mass flux out of the valley, when compared to that out of a valley of same volume but constant cross-sectional area.

The typical alpine landscape is not formed by single isolated valleys opening directly on plains. Valleys are usually connected to one another and are characterized by different geometries and land covers. The effects of neighboring valleys on the structure of the nocturnal

VBL and its evolution in a single valley section have received little attention to date. The overall aim of the present work is to quantify the impact of along-valley orographic variations (in a system of valleys) on the structure of the nocturnal VBL and its evolution in pooling and draining configurations. To meet this aim, high-resolution numerical simulations of idealized valleys in such configurations are performed.

This work is organized as follows: section 2 introduces the valley geometry, the definition of pooling and draining valleys, and the methodology used to compare valleys of different geometries, section 3 presents the design of the numerical simulations, the structure of the nocturnal VBL and its evolution are analyzed in section 4, the analysis of the valley heat budget is reported in sections 5 and 6, and conclusions are given in section 7.

2. Methodology

a. The idealized terrain

The idealized terrain considered in the present work can be thought as a system of two valleys of different cross-valley widths, connected to one another by a "junction," with one of the valleys opening on a plain $\mathscr{P}$. For the purpose of the discussion, the along-valley direction of the valley system is defined in this work as follows: because we consider nocturnal conditions, when the along-valley wind normally blows from the valley to the plain (that is down valley), the valley adjacent to the plain will be referred to as the downstream valley $\mathscr{V}_d$ and the valley farther from the plain will be referred to as the upstream valley $\mathscr{V}_u$. We restrict our attention to a system of valleys with flat valley floor. The system of valleys is made symmetric about the origin $(x, y) = (0, 0)$, where the cross-valley direction x is oriented west–east and the along-valley direction y is oriented south–north. The analytical expression for the terrain height h is given by

$$h(x,y) = Hh_x(x,y)h_y(y) + h_0, \tag{1}$$

where H is the height of the surrounding plateau, set to 800 m, and h_0 is a reference height, set to 1000 m.

The terrain height in the cross-valley direction x, denoted by h_x, is given by

$$h_x(x,y) = \begin{cases} \dfrac{1}{2} - \dfrac{1}{2}\cos\left[\pi\dfrac{|x| - L_x(y)}{S_x}\right] & L_x(y) \le |x| \le S_x + L_x(y) \\ 0 & |x| < L_x(y) \\ 1 & |x| > S_x + L_x(y) \end{cases}, \tag{2}$$

where S_x is the cross-valley slope width and L_x is the half-width of the valley floor. Terrain height h_x is made to vary continuously in the along-valley direction y by varying the half-width of the valley floor (along y) such that

$$L_x(y) = \frac{(L_{x,u} + L_{x,d})}{4\tanh\left(\dfrac{\alpha}{2}\right)}\left\{\tanh\left[\alpha\left(\frac{|y| - L_{y,u}}{L_J} - \frac{1}{2}\right)\right] + \tanh\left(\frac{\alpha}{2}\right)\right\}, \tag{3}$$

where $L_{y,u} = 10$ km is the length of $\mathscr{V}_u$, $L_J = 3$ km is the length of the junction that connects $\mathscr{V}_u$ to $\mathscr{V}_d$, and $L_{x,u}$ and $L_{x,d}$ are the half-width of the $\mathscr{V}_u$ floor and $\mathscr{V}_d$ floor, respectively. We set $\alpha = 5$, so that the half-width L_x in the $\mathscr{V}_u$ and $\mathscr{V}_d$ sections is approximately equal to $L_{x,u}$ and $L_{x,d}$, respectively.

The terrain height in the along-valley direction y, denoted by h_y, is defined as

$$h_y(y) = \begin{cases} \dfrac{1}{2} + \dfrac{1}{2}\cos\left(\pi\dfrac{|y| - L_{y,\mathrm{tot}}}{S_y}\right) & L_{y,\mathrm{tot}} < |y| \le S_y + L_{y,\mathrm{tot}} \\ 0 & |y| > L_{y,\mathrm{tot}} + S_y \\ 1 & |y| \le L_{y,\mathrm{tot}} \end{cases}, \tag{4}$$

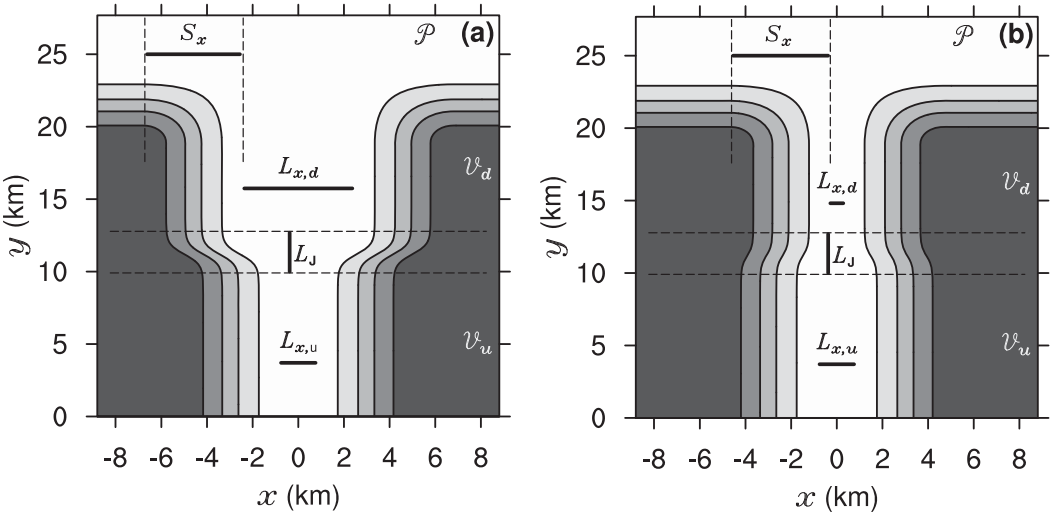

FIG. 1. Contours of the terrain height h (with intervals of 100 m) defined by Eq. (1). The cross-valley direction x is oriented west–east and the along-valley direction y is oriented south–north. The terrain is symmetric about the plane $y = 0$. (a) Draining case D1 in Table 1: upstream valley $\mathscr{V}_u$ ($0 < y < 10$ km) with half-width valley floor $L_{x,u}$, connected by a junction of length L_J to the downstream valley ($\mathscr{V}_d$, $13 < y < 19$ km) with half-width valley floor $L_{x,d} = 2.875L_{x,u}$, which opens on a plain $\mathscr{P}$. The cross-valley slope width S_x is the same for the downstream and upstream valleys. (b) Pooling case P1 in Table 1: as in (a), but considering a downstream valley with half-width valley floor $L_{x,d} = 0.25L_{x,u}$.

where $L_{y,\mathrm{tot}} = 24$ km is the total length of the valley system, $L_{y,d} = 6$ km is the length of $\mathscr{V}_d$, and $S_y = 5$ km is the along-valley slope width of $\mathscr{V}_d$.

This formulation for the terrain height can describe a valley opening or narrowing on another valley, which opens on a plain, as illustrated in Fig. 1. Figures 1a and 1b show contours of the terrain height h defined by Eq. (1) for $L_{x,d} = 2.875L_{x,u}$ and $L_{x,d} = 0.25L_{x,u}$, respectively.

b. *Definition of the pooling and draining configurations*

Following McKee and O'Neal (1989) and Whiteman (1990), the TAF of a cross-valley section with respect to the equivalent plain section is defined by the ratio

$$\Gamma = \frac{W_v H}{A_v}, \tag{5}$$

where W_v is the width of the valley at the height of the plateau H and A_v, is the cross-sectional area at fixed along-valley position y. The TAF can be calculated for different valley sections along the valley axis. If Γ decreases (i.e., the valley widens) in the down-valley direction, the valley is defined as a draining valley (see Fig. 1a); if Γ increases (i.e., the valley narrows) in the down-valley direction, the valley is defined as a pooling valley (see Fig. 1b). Hence, the ratio of the TAF between two cross-valley sections, termed the intravalley TAF and denoted by γ herein, characterizes the draining or pooling character of a valley; for instance, for $\mathscr{V}_u$ and $\mathscr{V}_d$, we get

$$\gamma = \frac{\Gamma_u}{\Gamma_d}, \tag{6}$$

where Γ_u and Γ_d are the topographic amplification factors for $\mathscr{V}_u$ and $\mathscr{V}_d$, respectively. Thus, we have $\gamma > 1$ for a draining valley and $\gamma < 1$ for a pooling valley.

With the parameters characterizing the valley geometry used in the present work, introduced in section 3, the width W_v of the valley at the height of the plateau H is given by $W_v(y) = 2[L_x(y) + S_x]$. The cross-sectional area A_v, at fixed along-valley position y, can be computed from the analytical expression for the terrain height in the cross-valley direction x [see Eq. (2)]. Integrating h for $-(S_x + L_x) < x < (S_x + L_x)$, and a fixed along-valley position y, where $h_y(y) = 1$, we get $A_v = H(2L_x + S_x)$. Hence, for the terrain geometry considered herein, Γ can be written explicitly as a function of L_x and S_x: $\Gamma = 2(1 + S_x/L_x)(2 + S_x/L_x)^{-1}$. Therefore, Γ is between 1 and 2, corresponding to the two limits $S_x/L_x \ll 1$ and $S_x/L_x \gg 1$, respectively.

For the valley geometry considered herein, γ is between 0.5 and 2. Contours of γ displayed in a $[(S_x/L_x)|_{\mathscr{V}_u}, (S_x/L_x)|_{\mathscr{V}_d}]$ diagram are shown in Fig. 2. For a deep and narrow (alpine) valley model, S_x/L_x should be larger than about 2 leading to γ between about 0.75 and 1.33. This shows that only a limited range of values for γ can be explored.

The geometrical parameters for the numerical simulations presented in this work are listed in Table 1. A symbolic notation is used to differentiate the simulations:

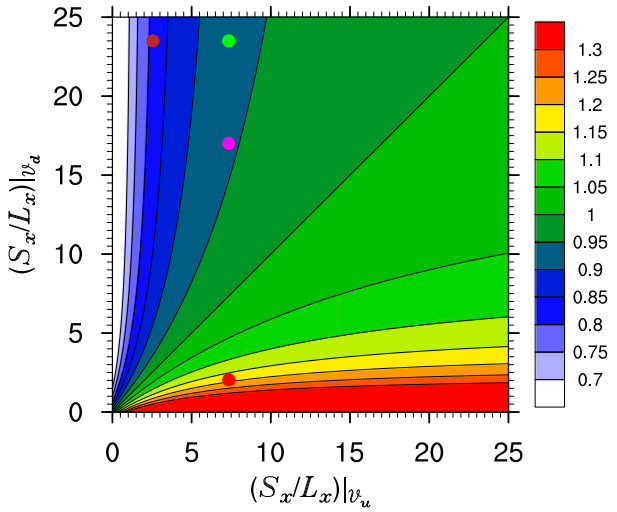

FIG. 2. Contours of $\gamma = \Gamma_u/\Gamma_d$, as a function of $(S_x/L_x)|_{\mathscr{V}_u}$ and $(S_x/L_x)|_{\mathscr{V}_d}$, where S_x is the slope length; L_x is the half-width of the valley floor; Γ_u and Γ_d are the topographic amplification factors for $\mathscr{V}_u$ and $\mathscr{V}_d$, respectively; and $\Gamma = W_v H/A_v$ with W_v the width of the valley at the height of the plateau H and A_v, the cross-sectional area at a fixed position in the along-valley direction. The color dots correspond to the cases considered in this work: D1 (red), P1 (green), P1b (magenta), and P2 (brown).

a capital letter X = I, D, or P defines the type of valley system [isolated valley–plain (I), draining (D), pooling (P)]; a number n = 1 or 2 defines the geometry of the upstream and reference valleys considered. The subscripts u and d are used to indicate the valley section considered (u for $\mathscr{V}_u$ and d for $\mathscr{V}_d$). For instance, P1$_d$ refers to $\mathscr{V}_d$ for the P1 case. A draining case (D1) and a pooling case (P1) will be compared to the isolated valley–plain I1 case. An additional case was simulated, referred to as P1b in Table 1, for which the parameters are the same as for the P1 case, except for $S_{x,d} = 3060$ m. The comparison between the P1 and the P1b cases elucidates the sensitivity of the $\mathscr{V}_u$ atmosphere to the ratio of the cross-sectional area of $\mathscr{V}_d$ to that of $\mathscr{V}_u$, denoted by R_V, while keeping γ almost constant (see Table 1). A limited range of pooling cases can be explored when considering the geometry for the I1 case. Therefore, another reference case (I2) is considered, for which $L_{x,u}$ is increased, allowing a pooling case characterized by a smaller value of γ. This pooling case will be referred to as the strong pooling case and denoted by P2. The along-valley variation of the cross-valley slope width S_x for the P1b case is obtained by applying a tanh function to S_x as is done for the half-width L_x, thereby leading to steeper slopes.

c. Heat budget

When examining the differential cooling along the valley, we consider the volume-averaged heat budget equation over a volume V_j (either in $\mathscr{V}_u$, $\mathscr{V}_d$, or $\mathscr{P}$); that is,

$$\frac{1}{V_j}\int_{V_j}\frac{\partial\theta}{\partial t}dV = \frac{1}{V_j}\int_{V_j} -u_i\frac{\partial\theta}{\partial x_i}dV + \frac{1}{V_j}\int_{V_j} -\frac{\partial s_i}{\partial x_i}dV + \frac{1}{V_j}\int_{V_j} -f\,dV. \tag{7}$$

The term on the left-hand side (lhs) of Eq. (8) is the volume-averaged potential temperature tendency, and the forcing terms on its right-hand side (rhs) are the volume-averaged potential temperature advection, divergence of the subgrid-scale (SGS) turbulent fluxes, and divergence of the radiative flux, respectively. Using Gauss's theorem and assuming incompressibility, the volume integrals of the advection and SGS turbulent flux divergence terms can be expressed as surface integrals, yielding

$$\underbrace{\frac{1}{V_j}\int_{V_j}\frac{\partial\theta}{\partial t}dV}_{T_j} = \frac{1}{V_j}\left(\underbrace{\int_{\Sigma_{j,i}} -a_i n_i\,d\Sigma + \int_{\Sigma_{j,i}} -\tau_i n_i\,d\Sigma}_{A_j} + \underbrace{\int_{\Sigma_{j,s}}\tau_s\,d\Sigma}_{S_j} + \underbrace{\int_{V_j} -f\,dV}_{F_j}\right), \tag{8}$$

where a_i and τ_i are the advective and SGS turbulent heat fluxes through the top and lateral surfaces $\Sigma_{j,i}$ of the volume V_j, respectively, n_i is the unit vector normal to the surfaces $\Sigma_{j,i}$ (defined positively outward), and τ_s is the sensible heat flux at the ground surface $\Sigma_{j,s}$.

We collect on the rhs the radiative flux divergence and surface sensible heat flux terms, which are responsible for the heat loss in the valley atmosphere. The sum of these two terms will be referred to as the diabatic term.

Herein the following notation is used:

$$X_{j,V_i} = \frac{1}{V_i}X_j, \quad \overline{X_j} = \int_{t_0}^{t_1} X_j\,dt,$$

where $X_j = T_j$, A_j, S_j, F_j and the volume V_i can be different from V_j.

TABLE 1. List of the numerical simulations performed in this study. A symbolic notation is used to differentiate the simulations, in which a capital letter X = I, D, and P defines the type of valley system [isolated valley–plain (I), draining (D), pooling (P)]; a number n = 1, 2 defines the geometry of the upstream and reference valleys considered. $L_{x,u}$ is the half-width floor of the upstream valley $\mathscr{V}_u$; $L_{x,d}$ is the half-width floor of the downstream valley $\mathscr{V}_d$; $S_{x,d}$ is the cross-valley slope width of the downstream valley; R_V is the ratio of the cross-sectional area of $\mathscr{V}_d$ to that of $\mathscr{V}_u$; Γ_u and Γ_d are the topographic amplification factor (TAF) of $\mathscr{V}_u$ and $\mathscr{V}_d$, respectively; and γ is the intravalley TAF between the two valley sections (e.g., the ratio of Γ_u to Γ_d). For all cases, $S_{x,u}$ = 4230 and H = 800 m. NA stands for nonappropriate.

Case	$L_{x,u}$ (m)	$L_{x,d}$ (m)	$S_{x,d}$ (m)	R_V	Γ_u	Γ_d	γ
I1	720	∞	4230	NA	1.74	1	1.74
D1	720	2070	4230	1.48	1.74	1.50	1.16
P1	720	180	4230	0.81	1.74	1.92	0.91
P1b	720	180	3060	0.60	1.74	1.89	0.92
I2	2070	∞	4230	NA	1.50	1	1.50
P2	2070	180	4230	0.55	1.50	1.92	0.78

Following Whiteman et al. (1996), we introduce a simple nondimensional form of the heat budget Eq. (8), based on the balance between T_{j,V_j} and A_{j,V_j} normalized by the diabatic term; that is,

$$\frac{T_{j,V_j}}{(S_{j,V_j}+F_{j,V_j})}-\frac{A_{j,V_j}}{(S_{j,V_j}+F_{j,V_j})}=1. \tag{9}$$

This equation can be interpreted physically as

$$\text{(Cooling efficiency)} + \text{(Draining efficiency)} = 1. \tag{10}$$

Indeed, the larger is the first term on the lhs of Eq. (9) when compared to the second term in absolute value, the larger is the fraction of the diabatic heat loss that contributes to cool the valley atmosphere. The first term on the lhs of Eq. (9) can thus be thought as a term measuring the "cooling efficiency" of the valley. By contrast, when the ratio of the advection terms to the diabatic term is equal to −1 for instance, the cooling within a valley section ceases even though the heat loss resulting from the diabatic term is nonzero. The second term on the lhs of Eq. (9) will be referred to as the draining efficiency; it is maximum when equal to −1.

When the cooling efficiency is larger than the draining efficiency in a valley, the valley is referred to as a trapper (Whiteman et al. 1996). If the reverse holds, the valley atmosphere is affected by advective warming, so reducing its overall cooling. This type of valley is referred to as a drainer. It is worth noting that Eq. (9) characterizes the behavior of valleys with internal variables (the heat budget terms), rather than with the geometry of the valley.

d. Comparison of the cumulative heat budget terms for different valley sections

In the following, we use the diagnostic framework introduced by Schmidli and Rotunno (2010), which separates the valley-volume effect from the thermodynamical processes controlling the valley heat budget when examining the differential cooling between an isolated valley and an adjacent plain.

Introducing the volume $P = W_v HY$ of the equivalent plain volume, the rhs of Eq. (8) can be rewritten as

$$T_{j,V_j}=\Gamma_j(A_{j,P}+S_{j,P}+F_{j,P}), \tag{11}$$

where Γ_j is the TAF of the upstream (for $j=u$) or downstream (for $j=d$) valley section of length Y in the along-valley direction, with respect to the equivalent plain section. Integrating Eq. (11), from a time t_0 to t yields $\overline{T_{j,V_j}}=\Gamma_j(\overline{A_{j,P}}+\overline{S_{j,P}}+\overline{F_{j,P}})$. The ratio of this latter expression for $\mathscr{V}_u$ to that for $\mathscr{V}_d$ for Y constant is a measure of the difference of the temperature changes from t_0 between $\mathscr{V}_u$ and $\mathscr{V}_d$. Collecting the diabatic term on the rhs yields

$$\frac{\overline{T_{u,V_u}}}{\overline{T_{d,V_d}}}=\gamma\frac{(\overline{S_{u,P_u}}+\overline{F_{u,P_u}})}{(\overline{S_{d,P_d}}+\overline{F_{d,P_d}})}\frac{\left[1+\dfrac{\overline{A_{u,P_u}}}{(\overline{S_{u,P_u}}+\overline{F_{u,P_u}})}\right]}{\left[1+\dfrac{\overline{A_{d,P_d}}}{(\overline{S_{d,P_d}}+\overline{F_{d,P_d}})}\right]}. \tag{12}$$

To simplify the notation, Eq. (12) is rewritten as

$$R_T=\gamma R_C R_A, \tag{13}$$

where R_T is the ratio of the net temperature changes and R_C and R_A are the ratios of the temperature changes due to the diabatic processes and advection, respectively, appropriately weighted by the respective plain volumes. Equation (13) allows the comparison of the heat budgets of different valley sections, separating the valley-volume effect from the differences in the thermodynamical processes. If the comparison is made between a valley section of volume V_j and an adjacent plain, Eq. (13) is equivalent to the one used by Schmidli and Rotunno (2010); that is,

$$R_T=\Gamma_j R_C R_A. \tag{14}$$

e. Definition of the control volumes and averaging

We set the length Y to 2 km. All the vertical profiles of the different fields shown in the next sections, if not specified otherwise, are horizontally averaged between $-180<x<180$ m and $2<y<4$ km and $14<y<16$ km

for the upstream and downstream valleys, respectively. These regions are termed the "valley center" areas (of $\mathscr{V}_u$ and $\mathscr{V}_d$, respectively). We shall also consider control volumes defined by $-(L_x + S_x) < x < (L_x + S_x)$, y in the ranges above, and $h_0 < z < H + h_0$. These volumes are denoted by V_u and V_d and will be termed "valley volume" regions. An average over such a control volume will be referred to as a valley-volume average. Control volumes for the isolated valley–plain configurations (I1 and I2) are defined as for V_u and V_d and will be termed V_I. Finally, a plain volume is defined by $-(L_x + S_x) < x < (L_x + S_x)$, $30 < y < 32$ km, and $h_0 < z < H + h_0$ and denoted by $\mathscr{P}$.

3. Numerical model setup

a. Numerical method

The numerical simulations reported in Table 1 were performed with the Weather Research and Forecasting (WRF) Model, version 3.4.1, using the ARW core (Skamarock et al. 2008). The WRF Model is a compressible, nonhydrostatic model, appropriate for scales ranging from meters to global scales. The governing equations are formulated using a terrain following hydrostatic-pressure coordinate and discretized on a staggered Arakawa-C grid. Advection terms were discretized using a fifth-order-weighted essentially nonoscillatory (WENO) scheme with positive definite filter. The time integration was performed with a third-order Runge–Kutta scheme, using the time-splitting technique described by Wicker and Skamarock (2002) for the acoustic mode. The subgrid scales were parameterized using a 1.5-order turbulent kinetic energy (TKE) scheme (Deardorff 1980). The Rapid Radiative Transfer Model (Mlawer et al. 1997) was used to parameterize the longwave radiation and the Dudhia (1989) scheme for the shortwave radiation. The surface forcing was simulated explicitly by coupling the atmospheric model to the Noah land surface model (Chen and Dudhia 2001) using the Monin–Obukhov similarity theory (the "MM5 revised" scheme; Jiménez et al. 2012). Shadowing effects were not taken into account in the present work.

b. Grid design

To prevent spurious numerical effects at the lateral boundaries, a large domain in the horizontal directions is needed. Two nested domains were used, with the inner domain covering the full valley system and part of the plain regions. Both domains were centered on the valley-system region. To minimize the errors at the lateral boundaries between the two domains, the ratio between the horizontal grid resolutions of the two domains was set to 3, and the number of grid points in the relaxation layer at the lateral boundaries of the inner domain was increased to 5 according to Moeng et al. (2007). The outer domain was discretized using 120 grid points in the x direction and 336 grid points in the y direction with a grid resolution $\Delta x|_{\mathrm{D1}} = \Delta y|_{\mathrm{D1}} = 270$ m. For the inner domain, 196 and 610 grid points were used in the x and y directions, respectively, with a grid resolution $\Delta x|_{\mathrm{D2}} = \Delta y|_{\mathrm{D2}} = 90$ m. The height of the domain was 12 km and 100 grid points were used along the vertical direction z for both domains. The vertical coordinate was stretched along the vertical using a hyperbolic tangent function, resulting in a resolution close to the ground of about 2 m, and vertical grid spacings continuously increasing with height. The time steps were 0.45 and 0.15 s for the outer and inner domains, respectively.

c. Initial conditions

The design of the initial conditions follows the setup of Burns and Chemel (2014). All the model runs were initialized 1 h before sunset, simulating a 6-h time period after that time, during wintertime. Because this study focuses on the development of stable boundary layers, postconvective conditions were considered for the initial base state, with the vertical gradient of virtual potential temperature θ set to 1.5 K km^{-1}. Even though highly idealized, such value of the lapse rate has been observed in mountainous region at sunset (e.g., Whiteman and Zhong 2008). For simplicity, θ will be referred as potential temperature thereafter. Its value at the valley floor was initialized to 288 K. The skin temperature was initialized by an extrapolation from the air temperature of the first three layers above ground level, and a random temperature perturbation with a minimum value of -0.05 K was applied to the skin temperature to reduce the spinup time of the simulation. To focus on the effects of the valley geometry on the circulation within the valley, the valley atmosphere was dynamically decoupled from the free atmosphere above by setting the wind speed to zero at the initial time across the domains. We restrict our attention to a relatively dry atmosphere, and so relative humidity was set to 40% across the domains, following previous setup of idealized cases (e.g., Schmidli 2013; Chemel and Burns 2015).

The soil properties and the land use were homogeneous in order to focus on the effects of the valley geometry. The land-use type was set to "grassland," which corresponds to short grass, a reasonable assumption for an alpine valley. The soil type was set to "silty clay loam"; the soil moisture was initialized so that it is 90% of the soil moisture content at field capacity. This is a value typical of conditions a few days after rainfall, which is a reasonable assumption given that wintertime is considered. The details of the soil initialization are reported in Burns and Chemel (2014).

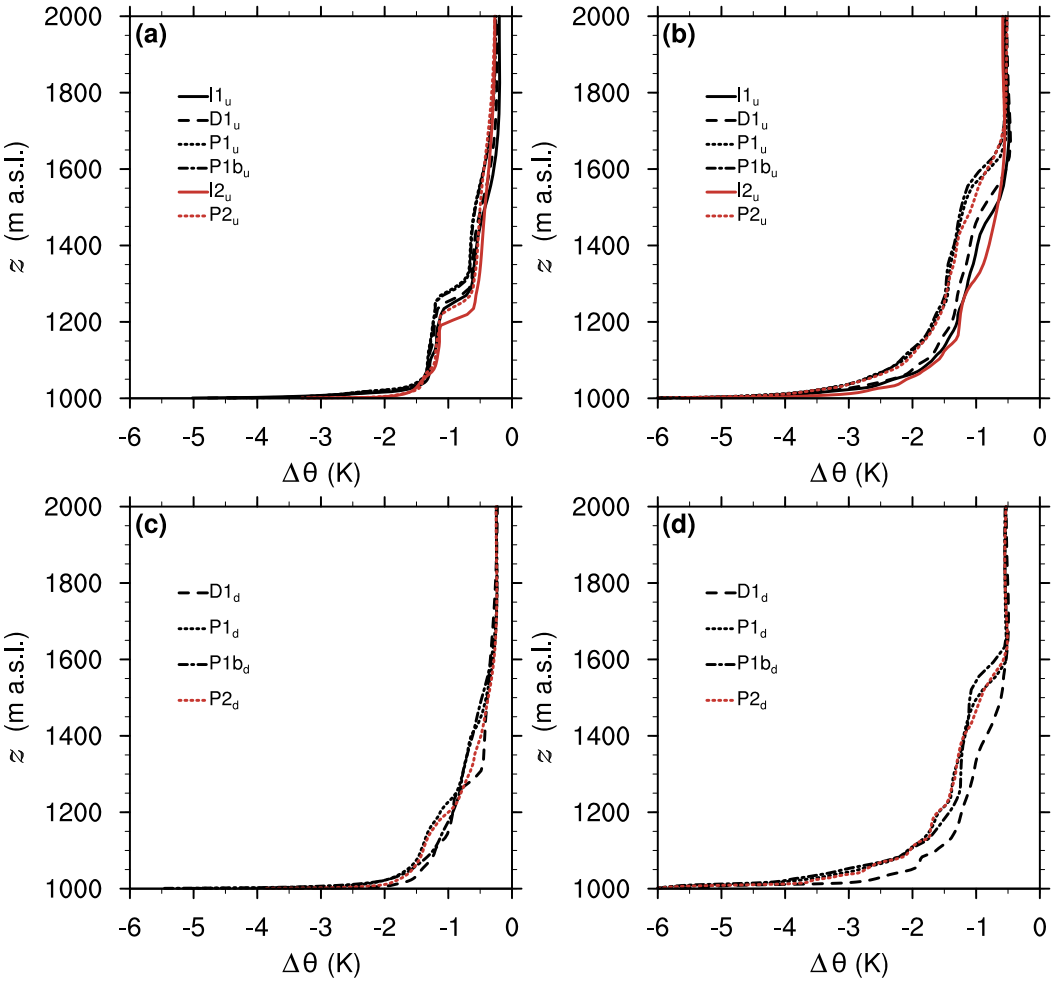

FIG. 3. (a) Vertical profiles of potential temperature change $\Delta\theta$ from $t = 0$ in the upstream valley, horizontally averaged in the range $-180 < x < 180$ m and $2 < y < 4$ km (in $\mathscr{V}_u$), at $t = 150$ min for the I1 (black solid line), D1 (black dashed line), P1 (black dotted line), I2 (red solid line), and P2 (red dotted line) cases; (b) as in (a), but at $t = 360$ min. (c) As in (a), but in the downstream valley, horizontally averaged in the range $-180 < x < 180$ m and $14 < y < 16$ km (in $\mathscr{V}_d$); (d) as in (c), but at $t = 360$ min; see Table 1 and section 2b for the definition of the simulations.

d. Boundary conditions

Periodic boundary conditions were imposed for the outer domain in the x direction. This is equivalent to having an infinite repetition of the same valley in this direction. Open boundary conditions were imposed in the y direction; because of the idealized setup and the duration of the simulations, only outflow at the boundaries in the y direction can be simulated. By increasing the number of grid points along y from 336 to 436 we verified that the flow in the region of interest is not affected by the open boundaries for this particular setup. The lateral boundaries of the inner domain were updated every outer domain time step. A sponge layer was introduced across the top 4 km of the domain to avoid any spurious effect of wave reflection on the numerical solution.

4. Thermal structure and flow evolution

The development of the down-valley flow depends on the differential cooling along the valley axis. In principle, the valley sections should cool differently because of the change of Γ along the valley axis. Because the valley sections are communicating, the down-valley flow transports mass and heat from $\mathscr{V}_u$ to $\mathscr{V}_d$ and to the plain, modifying this picture.

a. Thermal structure of the valley boundary layer

Figure 3 displays vertical profiles of potential temperature change from $t = 0$ in $\mathscr{V}_u$ and $\mathscr{V}_d$, denoted by $\Delta\theta$, for the different cases at $t = 150$ and 360 min. The top height of the VBL is diagnosed here by the top height of the elevated inversion layer. Figure 3a shows that the near-surface atmosphere experiences a strong cooling

during the first part of the night (θ decreases by 5 K from $t = 0$ to 150 min) for all the cases. The pooling cases P1 and P1b present a colder and deeper VBL than the respective reference case I1 and draining case D1; this result also holds for P2 and I2. As shown by Arduini et al. (2016), before the down-valley flow is fully developed, the depth of the VBL is controlled by the upward vertical transport induced by downslope flow convergence over the valley center. This vertical transport is suppressed by the development of the down-valley flow. As will be shown in section 4b, the development of the down-valley flow is delayed for the pooling cases with respect to the respective reference cases and with respect to the D1 case for the P1 and P1b cases. Hence, the vertical transport induced by the downslope flow convergence persists for a longer time in the pooling valleys, leading to a deeper VBL.

For the P1 and P2 cases, $\mathscr{V}_d$ presents a colder VBL than $\mathscr{V}_u$ for $z < 200$ m AGL (see Figs. 3a and 3c). Figure 3c also shows that the temperature difference between $\mathscr{V}_d$ and $\mathscr{V}_u$ is different for the P1 and P1b cases. For the P1b case, the atmosphere of $\mathscr{V}_d$ below $z = 200$ m AGL is slightly warmer than that for the P1 case, because the downslope flows that develop in $\mathscr{V}_d$ for the P1b case are weaker than those for the P1 case. Weaker downslope flows lead to a reduced sensible heat flux (since it is proportional to the near-surface wind speed) and, so, to a reduced cooling.

At $t = 360$ min, for $z > 100$ m AGL, $\mathscr{V}_d$ presents a warmer VBL than $\mathscr{V}_u$ for all the cases considered (see Fig. 3d); $\mathscr{V}_u$ for the D1, P1, P1b, and P2 cases generally presents a colder and deeper VBL than that for the respective reference cases (see Fig. 3b). Nonetheless, the degree of deviation from the reference cases changes between the draining and pooling cases. The thermal structure of $\mathscr{V}_u$ for the D1 case presents only small differences with that for the I1 case. Much deeper and colder boundary layers develop for the pooling cases. The case with the smallest value of γ (P2) presents the largest differences with the respective reference case (I2), with an increase of the boundary layer depth of 85%. The thermal structure of $\mathscr{V}_u$ is similar for the valley systems characterized by different geometries downstream but similar values of γ (P1 and P1b cases), suggesting that the thermal structure of $\mathscr{V}_u$ is independent of the volume of $\mathscr{V}_d$, as long as the TAF of $\mathscr{V}_d$ is unchanged.

Finally, it is worth noting that the atmosphere of $\mathscr{V}_u$ presents approximately the same vertical gradient of potential temperature in the upper part of the VBL (above the ground-based inversion) for all the cases by the end of the simulated time period, even though the atmosphere is generally colder for the valley-system cases. This suggests that the pooling or draining character of a valley does not substantially modify the atmospheric stability of the valley atmosphere above the ground-based inversion.

b. *Down-valley flow*

The differences in cooling of the valley atmosphere between the different configurations, shown in section 4a, have a substantial effect on the along-valley pressure gradient that ultimately drives the down-valley flow and, therefore, on the structure of the flow itself. Time series of the horizontally averaged near-surface down-valley wind speed at the exit of $\mathscr{V}_u$ and along-valley near-surface pressure difference between $\mathscr{V}_u$ and $\mathscr{V}_d$ are shown in Figs. 4a and 4b, respectively.

A low-level up-valley flow (i.e., negative values of the wind speed resulting from a negative pressure difference between $\mathscr{V}_u$ and $\mathscr{V}_d$) develops for the P1 and P2 cases during the first part of the night, while the thermally driven along-valley flow is normally down valley during the night (e.g., Zardi and Whiteman 2013). A similar unexpected behavior of the along-valley flow was observed by Whiteman et al. (1999) in subbasins of the Colorado River valley. The low-level up-valley wind is stronger as γ decreases and lasts until $t \simeq 105$ min for the P1 case and until $t \simeq 210$ min for the P2 case (see Fig. 4a). This is explained by the colder VBL for $z < 1200$ m in $\mathscr{V}_d$ than in $\mathscr{V}_u$ during these periods (see Figs. 3a and 3c). The near-surface down-valley flow for the P1b case does not present the same feature as for the P1 case during the early night; the near-surface pressure gradient barely changes sign and so an up-valley flow barely forms in this case. This is explained by the slightly warmer VBL in $\mathscr{V}_d$ for the P1b case than for the P1 case (see Figs. 3a and 3c).

The down-valley flow reaches a dynamical steady state by the end of the simulated time period for all the cases considered. When that steady state is reached, the near-surface down-valley wind speed is lower by at least a factor of 2 for the pooling and draining cases than for the respective reference cases. This reduction of the down-valley wind speed results from a reduction of the along-valley pressure gradient. The down-valley wind speed is also significantly smaller (40% smaller) for the pooling cases P1 and P1b than for the draining case. It is worth noting that the valley-to-plain pressure difference is smaller (and so is the down-valley wind speed) for the I2 case than for the I1 and D1 cases because the VBL is shallower (see Figs. 3a and 3b).

To investigate the characteristics of the down-valley wind speed along the vertical, vertical profiles of the wind speed at the same times as in Fig. 4 ($t = 150$ and 360 min) are shown in Fig. 5. At $t = 150$ min the up-valley

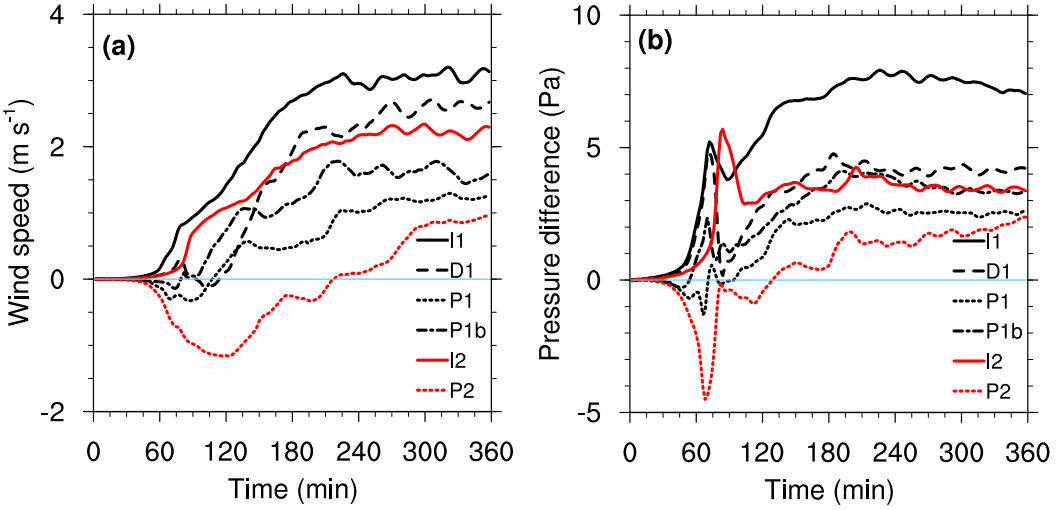

FIG. 4. (a) Time series of the down-valley wind speed at $z = 25$ m AGL, averaged in the range $-180 < x < 180$ m and $11 < y < 13$ km (i.e., $\mathscr{V}_u$ exit) and (b) horizontal pressure gradient between $\mathscr{V}_u$ and $\mathscr{V}_d$, computed along the valley axis at $y = 3$ km for $\mathscr{V}_u$ and $y = 13$ km for $\mathscr{V}_d$, at $z = 25$ m AGL, horizontally averaged in the range $-180 < x < 180$ m, for the I1 (black solid line), D1 (black dashed line), P1 (black dotted line), P1b (black dashed–dotted line), I2 (red solid line), and P2 (red dotted line) cases; see Table 1 and section 2b for the definition of the simulations.

flow in $\mathscr{V}_u$ for the P2 case fills the valley atmosphere up to the top of the VBL at this time (cf. Fig. 3a), reversing above. The other cases present qualitatively the same down-valley wind profiles, with a general reduction of the low-level (below 200 m AGL) wind speed when a downstream valley is present. At $t = 360$ min (see Fig. 5b), no up-valley flow is observed in the P2 case, in agreement with Fig. 4a. A distinction needs to be made between pooling and nonpooling cases. An antiwind is indeed present for the reference cases (and to some extent for the D1 case). By contrast, no antiwind forms for the pooling configurations within the valley, as the VBL is deeper in these cases and the down-valley flow fills the valley atmosphere almost up to the height of the plateau. Hence, mass conservation should be ensured by weak antiwinds above the plateau for these cases.

c. *Mass fluxes along the valley axis*

The differences in the down-valley flow that develops in the different configurations have an impact on the

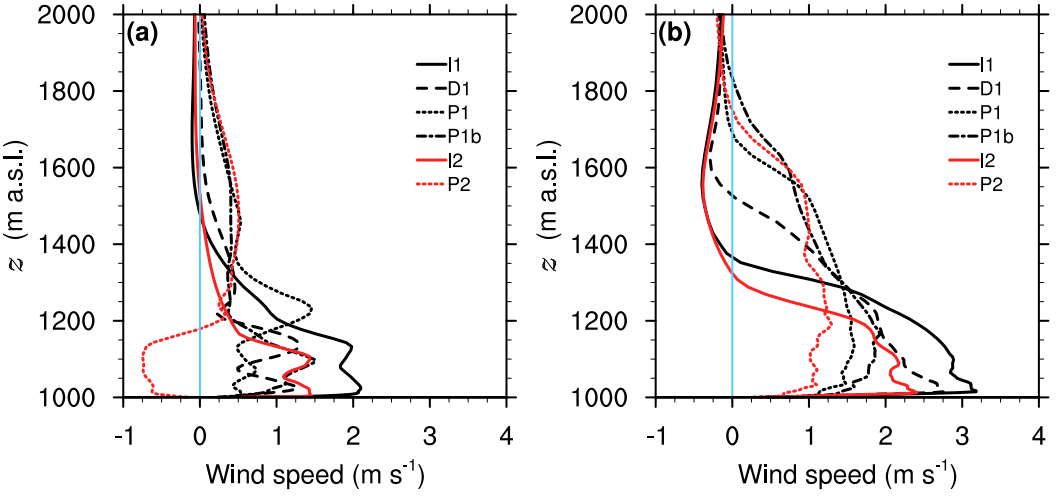

FIG. 5. (a) Vertical profiles of the down-valley wind component v, horizontally averaged in the range $-180 < x < 180$ m and $11 < y < 13$ km (i.e., $\mathscr{V}_u$ exit), at $t = 150$ min for the I1 (black solid line), D1 (black dashed line), P1 (black dotted line), I2 (red solid line), and P2 (red dotted line) cases; see Table 1 and section 2b for the definition of the simulations. (b) As in (a), but at $t = 360$ min.

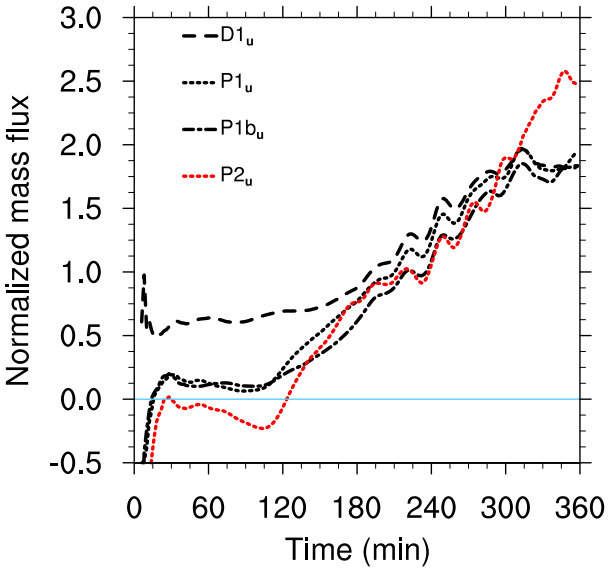

FIG. 6. Time series of the normalized net along-valley mass fluxes across the surfaces of the $\mathscr{V}_u$ valley volumes V_u, for the D1 (black dashed line), P1 (black dotted line), P1b (black dashed–dotted line), and P2 (red dotted line) cases; see Table 1 and section 2b for the definition of the simulations. The mass fluxes are normalized by the mass fluxes in the valleys for the respective reference cases (I1 and I2).

mass budget of $\mathscr{V}_u$. Figure 6 shows time series of the net along-valley mass fluxes in $\mathscr{V}_u$ for the D1, P1, P1b, and P2 cases, normalized by the net along-valley mass fluxes in the valleys for the respective reference cases (I1 and I2). All the mass fluxes are calculated across the along-valley surfaces of the volume V_u. Before t = 150 min, the mass fluxes are less than half those of the respective reference cases, indicating that the outflow of cold air from $\mathscr{V}_u$ is strongly reduced during the evening transition. The along-valley mass flux is negative in $\mathscr{V}_u$ until t = 120 min for the P2 case (the net mass flux being always positive for the I2 case), showing that there is a net flux of mass from $\mathscr{V}_d$ to $\mathscr{V}_u$ associated with the up-valley flow. It is worth noting that for the D1, P1, and P1b cases the values of the mass flux are similar after t = 180 min, despite the differences in the along-valley flow structure (see Fig. 5b). Although the low-level down-valley wind speed is reduced by a factor of 2 between the reference cases and the pooling cases (I1, and P1, P1b; I2 and P2) by the end of the simulated time period, the net along-valley mass flux is larger than that of the reference case by a factor of 2 for the P1 and P1b cases and by a factor of 2.5 for the P2 case. This is because of the presence of the return flow in the upper part of the valley atmosphere for the reference cases I1 and I2, which reduces the net along-valley mass flux out of V_u.

5. Heat budget of the upstream valley atmosphere

The differences in the thermal structure of the VBL in $\mathscr{V}_u$ between the different configurations, described in section 4a, are driven by the competing cooling processes described in section 2c. Here, we analyze in details the effects of the downstream valley on the cooling processes in the upstream valley, highlighting the differences with a reference valley opening directly on a plain.

a. *Instantaneous heat budget*

Figure 7 displays time series of the V_u-averaged terms of the heat budget equation [Eq. (8)] for the D1, P1, P1b, and P2 cases and the respective reference cases (I1 and I2). The control volumes over which the average is performed are defined in section 2e. The total cooling rate presents the same temporal evolution for all the cases: a transient regime characterized by a higher cooling rate, followed by a quasi-steady state with a lower cooling rate, which varies only slightly from case to case. As one would expect, the contribution of radiative flux divergence to the heat budget is not affected by the presence of the downstream valley, whatever the particular configuration considered. Hence, the differences in the temperature profiles observed in Fig. 3 are due to the differences in the advection and surface sensible heat flux contributions, which are affected by the orographic variations along the valley axis. The advection contribution from the SGS turbulent processes at the top-of-the-valley atmosphere and lateral boundaries is found to be negligible compared to that from the resolved motions (not shown). The duration of the transient regime increases as γ decreases (from the D1 to P2 cases; see Figs. 7a and 7c), thereby delaying the time when the advection contribution reaches a steady state. When the steady state is reached, the contributions from advection and surface sensible heat flux differ from case to case, but the sum of the two does not. This is because weaker down-valley flows lead to a reduction of the contributions from both advection and sensible heat flux (in absolute value). Hence, the cooling rate is almost equal for all the cases considered by the end of the simulated time period.

b. *Heat transport in and out of the valley*

The heat fluxes that determine the heat transport in and out of $\mathscr{V}_u$ are those across the surfaces of V_u normal to the valley axis and across the upper surface of V_u. The calculation of the heat fluxes across the surfaces has to be done with respect to a physically based reference temperature in order to get meaningful information (Lee et al. 2004). Because the heat budget terms are

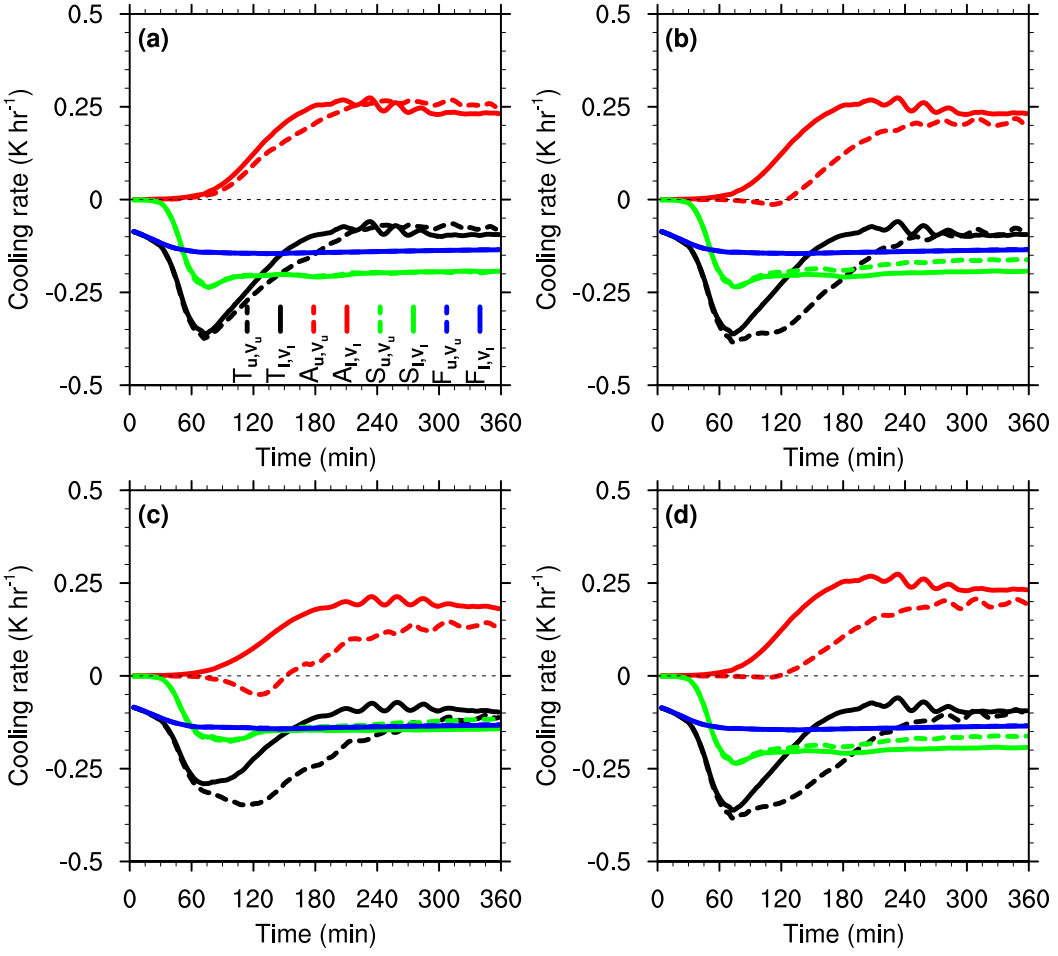

FIG. 7. Time series of the valley-volume-averaged terms of the heat budget equation [(total) tendency T, advection A, surface sensible heat flux S, radiative flux divergence F; see Eq. (8)] for the upstream valley (dashed line) and the corresponding isolated valley opening directly on a plain (continuous line) for the (a) D1, I1; (b) P1, I1; (c) P2, I2; and (d) P1b, I1 cases; see Table 1 and section 2b for the definition of the simulations.

averaged over the valley volume, the potential temperature averaged over that volume is used as the reference temperature.

Figure 8 displays time series of along-valley and vertical heat fluxes for $\mathscr{V}_u$, for the D1, P1, P1b, and P2 cases and the respective reference cases (I1 and I2). For the I1 and I2 cases, the contribution from the net along-valley heat flux increases with time, and it is 82% and 88%, respectively, of the total advection contribution by the end of the simulated time period (see Figs. 8a and 8c). For the D1 case the along-valley heat flux is reduced, and it is 60% of the total advection contribution by the end of the simulated time period (see Fig. 8a). This indicates that the net export of colder air out of $\mathscr{V}_u$ by the down-valley flow is the most efficient heat transport mechanism for the draining and reference cases. However, the vertical heat flux plays a nonnegligible role for the D1 case, and it is increased by a factor of 2.4 compared to that for the respective reference case. For the pooling cases, the net along-valley heat flux accounts for 32% of the contribution from advection for the P1 and P1b cases and 15% for the P2 case at the end of the simulated time period (see Figs. 8b–d). This indicates that the import of warmer air at the valley top is the dominant heat transport mechanism for the pooling cases. Compared to those for the respective reference cases, the vertical heat flux is increased by a factor of 3.2 for the P1 and P1b cases and by a factor of 5.3 for the P2 case.

The larger value of the vertical heat flux for the pooling and draining cases can be explained as follows: $\mathscr{V}_u$ for the pooling and to some extent the draining cases do not present significant antiwinds because of the deeper VBL. Hence, the mass in $\mathscr{V}_u$ for these cases is conserved only by downward vertical motions at the valley top. Using mass conservation in the upstream

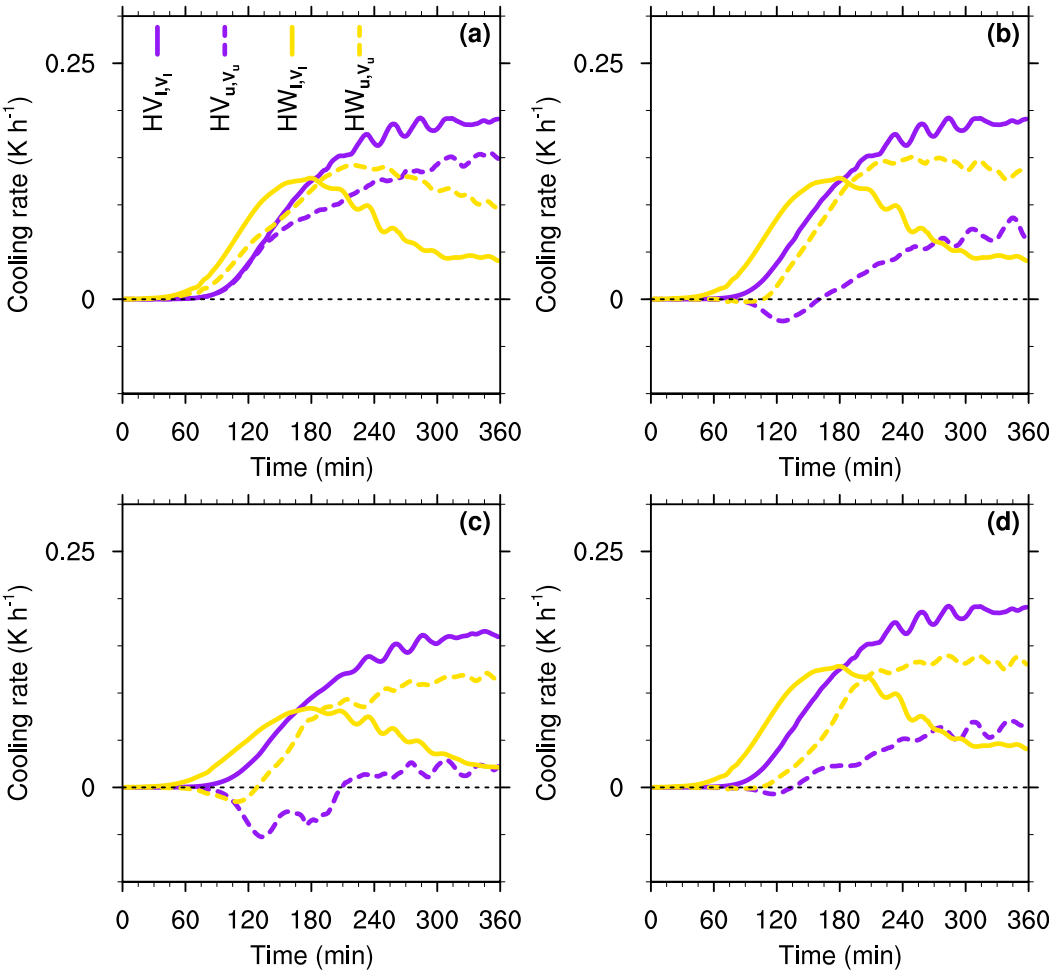

FIG. 8. Time series of the net horizontal (along valley) heat flux (HV) and vertical heat flux (HW) across the surfaces of V_u for the upstream valley (dashed line) and the corresponding isolated valley opening directly on a plain (continuous line) for the (a) D1, I1; (b) P1, I1; (c) P2, I2; and (d) P1b, I1 cases; see Table 1 and section 2b for the definition of the simulations.

valley, it is inferred from Fig. 6 that the downward vertical mass flux is 1.8 times larger for the D1, P1, and P1b cases than for the I1 case and 2.5 times larger for the P2 case than for the I2 case. In addition, the V_u-averaged temperature is lower for the pooling and draining cases than that for the respective reference cases; hence, the vertical heat flux calculated with respect to this reference temperature is larger, provided that the atmosphere is stably stratified and that the temperature at the valley top is the same for all the cases considered (as it is the case here; see Fig. 3). The increased downward vertical motions and larger temperature deficit combined explain the larger vertical heat flux across the valley-top surface when compared with that of the respective reference cases. The same arguments can be used for the P2 case to account for the larger vertical heat flux relative to the net along-valley heat flux. In summary, when considering $\mathscr{T}_u$ for the pooling and draining cases, the net heat flux in the along-valley direction is reduced when compared to those for the respective reference cases, in particular during the transient regime, enhancing the V_u-averaged valley cooling during this time. This results in a stronger vertical heat flux at the valley top, which in turn advects warmer air diminishing the V_u-averaged valley cooling when a quasi-steady state is reached.

c. *Draining versus cooling efficiency*

Further insight into the respective contributions of the diabatic and advective terms in the heat budget equation [Eq. (8)] for $\mathscr{T}_u$ for the different cases considered can be obtained by comparing the cooling and draining efficiencies introduced in Eqs. (9) and (10). Whiteman et al. (1996) proposed a comparison of draining efficiency

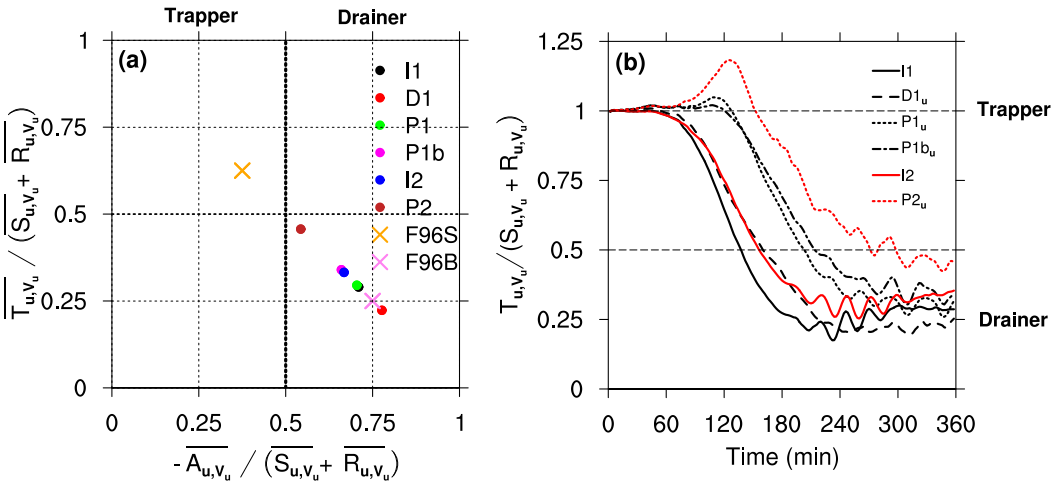

FIG. 9. (a) Heat budget diagram based on Eq. (9) for the upstream valley, for all the configurations simulated; see Table 1 and section 2b for the definition of the simulations. The terms of the heat budget are valley volume and time averaged between $t = 300$ and 360 min. For comparison, the values computed for the Colorado's Sinbad basin (F96S marker) and the Brush Creek valley (F96B marker) by Fast et al. (1996), averaged over the full nighttime period, are reported. (b) Time series of the ratio of the (total) tendency to the diabatic term for the upstream valley, with the terms of the heat budget averaged over the valley volume, for the I1 (black solid line), D1 (black dashed line), P1 (black dotted line), P1b (black dashed–dotted line), I2 (red solid line), and P2 (red dotted line) cases.

versus cooling efficiency for the nighttime period, when a quasi-steady state is reached. This representation allows a direct and quantitative comparison with other valleys and basins. Figure 9a shows draining efficiency versus cooling efficiency with the terms of the heat budget valley-volume averaged and time averaged over the last hour of the simulations (i.e., between $t =$ 300 and 360 min), when the quasi-steady state is reached. As references, the nighttime values calculated for the Sinbad basin and the Brush Creek valley (Fast et al. 1996) are also displayed.

From Eq. (9), all cases are located on the main diagonal of Fig. 9a. We will refer to $\mathscr{T}_u$ as a drainer if the case belongs to the lower (right) quadrant and as a trapper if it belongs to the upper (left) quadrant. The draining case D1 is characterized by a smaller value of the cooling efficiency than the I1 case during the quasi-steady state, indicating that the draining character of a valley is associated with a lower cooling efficiency. The value for the D1 case is very similar to the one computed for the Brush Creek valley, which was classified as a drainer by Whiteman et al. (1996). Figure 9a indicates that the stronger the pooling character, the higher is the cooling efficiency of the valley. Yet, pooling configurations do not fall in the trapper quadrant, implying that a valley characterization based on the intravalley TAF (γ) only can be misleading. For instance, the value of the cooling efficiency for $\gamma = 0.79$ (for the P2 case) is only 0.46 during the quasi-steady state, because the contribution from advection is still large compared to that from the diabatic term. It is worth reporting that the development of a down-valley flow does not prevent a valley from behaving as a trapper. Fast et al. (1996) indeed observed a considerable mass flux out of the Sinbad basin during the period of analysis, despite its trapper character.

The characterization of the valleys based on this diagram is valid strictly only when a steady state is reached. Figure 9b shows time series of the cooling efficiency of $\mathscr{T}_u$ with the terms of the heat budget averaged over the valley volume. During the first 2 h of the simulations (i.e., during the evening transition), all the valleys behave as a trapper, since the along-valley flow is not fully developed yet, then "sliding down" on the diagram (as the cooling efficiency decreases), eventually reaching a position characterizing their quasi-steady state for the rest of the night. Once the cooling efficiency starts to decrease, the speed of the descent (the rate of change of the cooling efficiency) is remarkably independent of γ. However, a shift in time and a difference in amplitude are apparent between the different cases, which make both the position (on the diagram) of the steady state and the time to reach it dependent on γ. It is worth noting that the I2 case presents a greater cooling efficiency than the I1 case during the entire simulated time period. However both cases behave as a drainer, implying that the valley width in the case of an isolated valley opening on a plain does not influence the drainer character of the valley. Finally, in this representation the P1b case hardly differs from the P1 case (taking into account that the ratio of the volumes of $\mathscr{T}_d$ and $\mathscr{T}_u$ for

the P1b case is closer to that for the P2 case than that for the P1 case; see Table 1). Hence, for the range of values for γ considered, we can conclude that the intravalley-volume effect explains to a certain extent the influence of the downstream valley on the trapper or drainer character of the upstream valley.

6. Along-valley variations of the heat budget

In the following sections, the cooling processes in the upstream and downstream valleys are compared, elucidating their impact on the heat budget of the valley system.

a. *Instantaneous heat budget of the upstream and downstream valleys*

Figure 10 shows time series of the valley-volume-averaged terms of the heat budget [Eq. (8)] and of the net along-valley and vertical heat fluxes across the surfaces of the volumes for $\mathscr{V}_u$ and $\mathscr{V}_d$, for the D1, P1 and P2 cases, and the total cooling (tendency term) averaged over the plain volume. For $t < 60$ min, Fig. 10c and Fig. 10e show that for the pooling cases (P1 and P2), $\mathscr{V}_d$ experiences a stronger cooling than $\mathscr{V}_u$. This stronger cooling stems from the cooling contribution from the surface sensible heat flux, which is larger in the narrower valley because of the smaller valley volume. During this time period, the warming effect from advection has not started yet (see Figs. 10c and 10e). Hence, the atmosphere is cooler in $\mathscr{V}_d$ than in $\mathscr{V}_u$, forcing the up-valley flow from $\mathscr{V}_d$ to $\mathscr{V}_u$ (most noticeable for the P2 case).

After this initial period and for the rest of the simulated time, the surface sensible heat flux contribution to the valley heat budget for $\mathscr{V}_u$ and $\mathscr{V}_d$ evolves similarly in time, whatever the case considered, with an almost constant offset between each other. The sign of this offset is reversed for the pooling and draining cases because the surface sensible heat flux is larger in the narrower valleys.

In regard to the advection contribution, its temporal evolution differs from case to case. For the draining case D1, the advection contribution for $\mathscr{V}_d$ follows that for $\mathscr{V}_u$ (see Fig. 10a), with a slightly greater warming in $\mathscr{V}_u$ than in $\mathscr{V}_d$ after $t \simeq 90$ min. This can be explained as follows: the along-valley heat flux hardly varies between $\mathscr{V}_u$ and $\mathscr{V}_d$ (see Fig. 10b); by contrast, at the end of the simulated time period, the vertical heat flux at the valley top is about 2 times larger in $\mathscr{V}_u$ than in $\mathscr{V}_d$, these fluxes being smaller than their along-valley counterparts by a factor of 1.5 (in $\mathscr{V}_u$) and 3 (in $\mathscr{V}_d$).

For the pooling cases the advection contribution for $\mathscr{V}_d$ increases rapidly during the transient regime (after 60 min; see Fig. 10c for the P1 case and Fig. 10e for the P2 case), because of the transport of cold air out of $\mathscr{V}_d$ by the down-valley flow toward the plain and the up-valley flow toward $\mathscr{V}_u$, and the resulting downward transport of warm air at the valley top (see Figs. 10d and 10f). For $\mathscr{V}_u$, the advection contribution becomes positive and increases after $t \simeq 120$ min for the P1 case and $t \simeq 150$ min for the P2 case. This is due to the vertical heat flux that increases rapidly at those times, while the along-valley heat flux is negative. The difference between the advection contributions for $\mathscr{V}_u$ and $\mathscr{V}_d$ exceeds that between the surface sensible heat flux contributions for $60 < t < 185$ min for the P1 case and $70 < t < 210$ min for the P2 case, leading to a higher cooling rate in $\mathscr{V}_u$. This leads to a reversal of the pressure gradient and so a down-valley flow develops from $\mathscr{V}_u$ to $\mathscr{V}_d$.

When a quasi-steady state is reached, for the P1 case, the vertical heat flux is 50% larger in $\mathscr{V}_u$ than in $\mathscr{V}_d$, while the along-valley heat flux in $\mathscr{V}_u$ is about 2.5 smaller that in $\mathscr{V}_d$. For the P2 case the vertical heat flux is 30% larger in $\mathscr{V}_u$ than in $\mathscr{V}_d$, while the along-valley heat flux in $\mathscr{V}_u$ is about 8 times smaller than in $\mathscr{V}_d$. This shows that the difference between the advection contribution for $\mathscr{V}_u$ and $\mathscr{V}_d$ for the pooling cases is due largely to the reduction of the along-valley heat flux in $\mathscr{V}_u$.

The development of the down-valley flow leads to the homogenization of the cooling rate in the along-valley direction after 210 min, whatever the case considered. This homogenization of the cooling rate results from a balance between advection and surface sensible heat flux: a greater contribution from advection for $\mathscr{V}_u$ than for $\mathscr{V}_d$ (as for the D1 case) goes along with a greater (in absolute value) contribution from the surface sensible heat flux. Conversely, when the contribution from advection is smaller for $\mathscr{V}_u$ than for $\mathscr{V}_d$ (as for the P1 and P2 cases), the contribution from the surface sensible heat flux is also smaller (in absolute value). These aspects are discussed in the next section using volume arguments.

b. *Time-integrated valley heat budget*

The left column of Fig. 11 shows the along-valley variability of the cooling processes, using the ratios of the time-integrated terms of the heat budget of $\mathscr{V}_u$ to those of $\mathscr{V}_d$ weighted by the plain volume [see Eq. (13)], for the D1, P1, and the P2 cases. The time integration starts at the beginning of the simulation. For all the cases the ratio R_C of the sum of the diabatic forcing terms for $\mathscr{V}_u$ to that for $\mathscr{V}_d$ hardly differs from one after a rapid adjustment at the beginning of the simulations (first 30 min). This suggests that, for the range of parameters considered, the heat loss from the diabatic term, weighted by the volumes of the respective equivalent plains, is unchanged along the valley axis. The advection

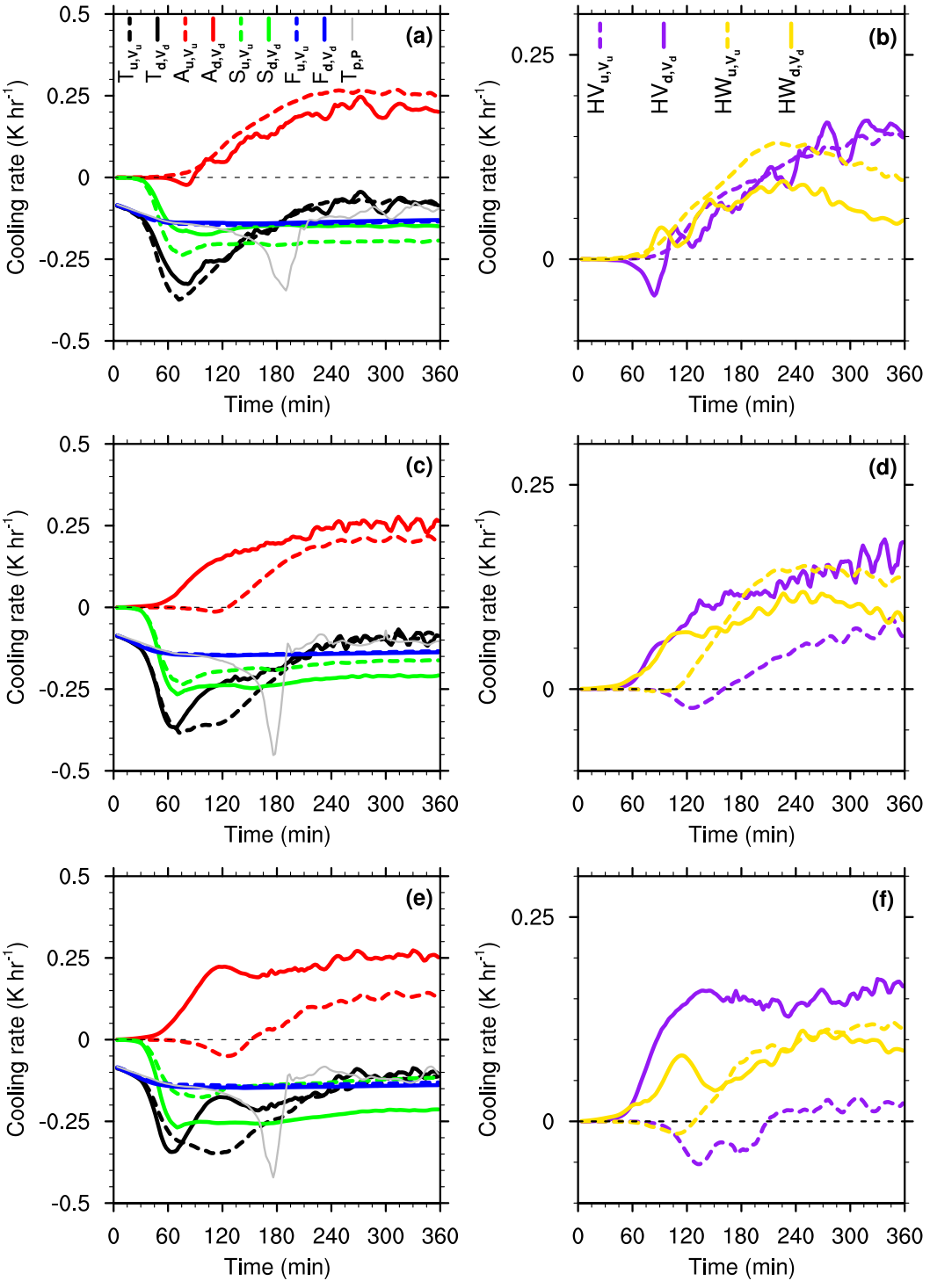

FIG. 10. (left) Time series of the terms of the valley heat budget [see Eq. (8)] for the upstream (dashed line) and downstream (continuous line) valleys for the (a) D1, (c) P1, and (e) P2 cases; see Table 1 and section 2b for the definition of the simulations. (right) Net horizontal (along valley) heat flux (HV) and vertical heat flux (HW) across the surfaces of V_u and V_d for the upstream (dashed line) and downstream (continuous line) valleys for the (b) D1, (d) P1, and (f) P2 cases. The gray line corresponds to the total cooling (tendency term) for the plain volume, defined by $-(L_{x,u} + S_{x,u}) < x < (L_{x,u} + S_{x,u})$, $30 < y$ 32 km, and $h_0 < z < H + h_0$.

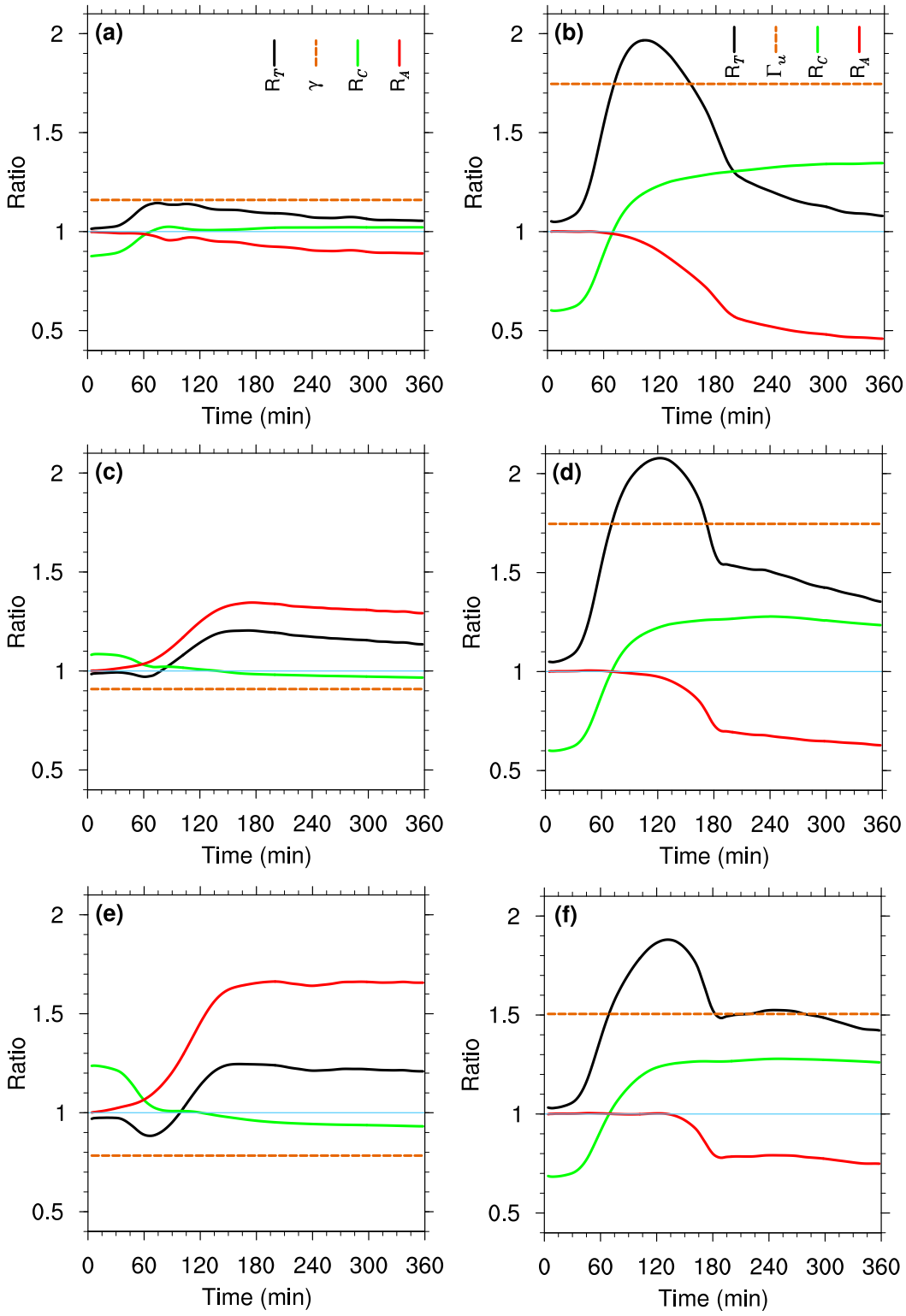

FIG. 11. (left) Ratios of the time-integrated terms of the heat budget of the upstream valley to those of the downstream valley [see Eq. (13)], for the (a) D1, (c) P1, and (e) P2 cases; see Table 1 and section 2b for the definition of the simulations. (right) The same ratios, but considering the upstream valley and the plain [see Eq. (14)] for the (b) D1, (d) P1, and (f) P2 cases. The plain volume is defined as in Fig. 10.

contribution to the heat budget is similar (and almost negligible) for $\mathscr{V}_u$ and $\mathscr{V}_d$ during the initial period ($t <$ 60 min for the pooling cases, $t < 100$ min for the draining case; see Fig. 10). Hence, the lower (higher) cooling rate in $\mathscr{V}_u$ with respect to that in $\mathscr{V}_d$ for the pooling (draining) cases is in large part explained by the intravalley-volume effect. This result holds also for the P1b case (not shown). However, it should be noted that R_C decreases slightly with time for the pooling cases (see Figs. 11c and 11e) because of the weaker down-valley wind speed in $\mathscr{V}_u$, which reduces the surface sensible heat flux and so the surface sensible heat flux component of R_C. The importance of this process for values of γ smaller than the ones considered in this study needs to be evaluated in future work.

The ratio of the advection contributions to the valley heat budget for $\mathscr{V}_u$ and $\mathscr{V}_d$, denoted as R_A, may be interpreted as follows: recalling the change in the cooling efficiency of valleys of different widths, wider valleys are characterized by a higher cooling efficiency when compared to narrower valleys, for the range of parameters studied (see the position of the I1 and I2 cases in Fig. 9a), yielding $R_A < 1$ for the D1 case (see Fig. 11a) and $R_A > 1$ for the P1 case (see Fig. 11c) and the P2 case (see Fig. 11e). It is worth noting that for the pooling cases the product γR_A is larger than 1; since $R_C \simeq 1$, this leads to a larger temperature change from $t = 0$ in $\mathscr{V}_u$ than in $\mathscr{V}_d$ (R_T), forcing the development of the down-valley flow from $\mathscr{V}_u$ to $\mathscr{V}_d$.

The right column of Fig. 11 shows the variability of the cooling processes in $\mathscr{V}_u$ with respect to the plain, using the same ratios used for the left column, but considering the plain volume instead of $\mathscr{V}_d$ [see Eq. (14)], for the same cases (D1, P1, and P2). As already shown by Schmidli and Rotunno (2010) for a valley–plain configuration, the higher cooling experienced by the valley with respect to the plain during the transient regime can be in large part explained by the valley-volume effect. However, as opposed to the intravalley analysis, R_C substantially differs from one. As shown by Arduini et al. (2016), downslope flows are the main driver of the surface sensible heat flux, so that the contribution of the surface sensible heat flux to the heat budget is necessarily different between the valley and the plain for quiescent synoptic conditions. After the down-valley flow has developed, the thermally driven circulation acts in order to reduce the temperature contrast between the valley and the plain, through the advection term R_A (smaller than 1), which can be considered the result of the transfer of cold air from the valley to the plain. This process is most efficient for the D1 case, where $R_A = 0.46$ by the end of the simulated time period (see Fig. 11b), leading to a nearly constant temperature difference between the valley and the plain of about 10%. This process is less effective as γ decreases (from the D1 to P2 cases; see Figs. 11c and 11e), because the heat transfer from $\mathscr{V}_u$ to the plain volume is reduced by the valley constriction. Interestingly, for the P2 case the temperature difference between $\mathscr{V}_u$ and the plain follows Γ once the down-valley flow has developed (that is after $t \simeq 180$ min); this is the result of the product $R_A R_C$ being almost equal to 1.

7. Conclusions

The purpose of this work was to quantify the impact of along-valley variations of the valley width on the nocturnal boundary layer structure of deep valleys, considering systems of two valleys: one upstream, one downstream, opening on a plain. The work shows that the dynamical and thermodynamical properties of the nocturnal valley boundary layer of a valley section are strongly affected by the valley width of the neighboring valleys. Three main configurations are considered: a draining case, a moderate pooling case, and a strong pooling case, which are compared to reference cases for which the upstream valley opens directly on a plain. The key findings, for the range of parameters considered, are summarized below for the upstream valley, unless otherwise stated:

- Draining and pooling configurations induce deeper and colder valley boundary layers compared to valleys opening directly on a plain (see Fig. 3). This effect is more pronounced for the pooling configurations.
- The along-valley variations of the valley width lead to a general decrease of the low-level down-valley wind speed when compared to a valley–plain configuration. This reduction of the wind speed results from a reduction of the along-valley pressure gradient that ultimately drives the down-valley flow (see Figs. 4a and 4b). The deeper valley boundary layer in the pooling configurations leads to a deeper down-valley flow, with no antiwinds up to the plateaus, as opposed to the valley–plain configuration. Because of the absence of antiwinds, the net mass flux out of the valley is higher in pooling and draining configurations when compared to the corresponding valley–plain configurations (see Fig. 6), although the low-level down-valley wind is reduced by a factor of 2. For the strong pooling configuration, the mass flux is up-valley during the early night, leading to an inflow of air from the downstream to the upstream valley.
- For all the configurations considered, a steady state is reached, but the duration of the transient regime depends on the configuration. This duration is shortest for the draining and valley–plain configurations. For the pooling configurations, it increases as the valley becomes narrower in the down-valley direction (i.e., the

intravalley topographic factor γ decreases). As pointed out by previous studies (e.g., Burns and Chemel 2015; Arduini et al. 2016), the growth of the valley boundary layer is mainly controlled by the vertical motions induced by downslope flows within the valley center. Hence, the transient regime is responsible for the differences in the thermal structure of the atmosphere of the different valleys.

- For the draining configuration the cooling processes in the upstream valley are comparable to those of the corresponding valley–plain configuration and, so, are hardly affected by the presence of the downstream valley (see Fig. 7a). For the pooling configurations the cooling rate is about 50% larger than that of the corresponding valley–plain configurations during the transient regime because of the reduction of the along-valley and vertical heat fluxes during this time period (see Figs. 8b–d). When a steady state is reached, the advection contribution to the valley heat budget leads to a warming of the valley atmosphere. It is dominated by the along-valley heat flux for the draining and valley–plain configurations and by the vertical heat flux at the valley top for the pooling configurations.
- By comparing the quasi-steady state for the upstream valleys, we conclude that a pooling valley is not necessarily a ''trapper'' in the Whiteman et al. (1996) classification (see Fig. 9a), this classification being strictly valid only when a steady state is reached. In other words, $\gamma < 1$ is not a sufficient condition to have a trapper for the entire night. Note that, when examining the trapper or drainer character of the valley during the evening transition, namely before the steady state is reached, all the valleys behave as a trapper and then evolve toward a drainer state when the down-valley flow develops (see Fig. 9b). It is found that, as soon as the down-valley flow develops, the rate at which the steady state is reached is independent of γ, while the time when the down-valley wind develops and the cooling rate during the quasi-steady state are dependent on γ.
- The effect of the along-valley flow is to reduce the horizontal temperature gradients resulting from the variations of the valley width along the valley axis. Once the down-valley flow is fully developed, all valleys present a homogeneous cooling rate in the along-valley direction (see Fig. 10). The diabatic forcing term of the valley heat budget (defined as the sum of the radiative flux divergence and the surface sensible heat flux), when weighted by the volume of the respective equivalent plains, hardly varies between different valley sections [as was assumed in McKee and O'Neal (1989)], with minor differences resulting from the differences in the down-valley wind speed between the two adjacent valleys (see Fig. 11, left column). Therefore the difference in the temperature change from $t = 0$ between the two valley sections is driven by that during the transient regimes in the two valleys. Hence, it is driven by the value of γ and the ratio R_A of the advection contribution (to the valley heat budget) for $\mathscr{V}_u$ to that for $\mathscr{V}_d$: $\gamma > 1$ and $R_A < 1$ for the draining configuration, and $\gamma < 1$ and $R_A > 1$ for the pooling configurations. Since for the pooling configurations the product γR_A is larger than 1, the valley boundary layer in the upstream valley is colder than that in the downstream valley (after the dynamics in the valleys are established), leading to the formation of the down-valley flow from the upstream to downstream valleys.
- For the considered quiescent synoptic conditions, the assumption that the diabatic forcing term has the same amplitude within the valley and over the plain is not valid during nighttime for the deep valley considered here. Indeed, the diabatic forcing term is larger within the valley than over the plain, thus enhancing the temperature contrast between the valley and the plain (see Fig. 11, right column). The development of the down-valley flow reduces this temperature contrast. This reduction cannot be explained by the valley-volume effect. It is slowed down for the pooling configurations because of the reduced heat flux out of the valley. It is found that for the strong pooling configuration the valley-volume effect explains the differential cooling between the valley and the plain once the down-valley flow has developed. In the absence of significant dynamical processes, the valley–plain (bulk) temperature differences can possibly be quantified by the topographic amplification factor. Our results also suggest that this condition can be reached in a valley subject to dynamical processes, when the cooling resulting from the surface sensible heat flux within the valley compensates the warming due to advection; the along-valley constriction is key to reaching this balance.

The results reported here concern a small fraction of possible configurations. Other parameters of particular importance that have not been considered in this study include the shape of the cross-valley slopes along the valley axis and the height of the terrain, which would both affect the topographic amplification factor of the valley (valley-volume effect) and downslope flows (dynamical effects). A characterization of the effects of the full range of orographic variations along the valley axis is needed in order to understand and predict the evolution of the boundary layer of a particular valley section.

Acknowledgments. This work has been supported by a Ph.D. grant provided by the LabEx Osug@2020 (Investissements d'avenir–ANR10LABX56) in Grenoble and

by the University of Hertfordshire. Numerical simulations were run on the French national HPC facilities at CINES.

REFERENCES

Arduini, G., C. Staquet, and C. Chemel, 2016: Interactions between the nighttime valley-wind system and a developing cold-air pool. *Bound.-Layer Meteor.*, **161**, 49–72, doi:10.1007/s10546-016-0155-8.

Burns, P., and C. Chemel, 2014: Evolution of cold-air-pooling processes in complex terrain. *Bound.-Layer Meteor.*, **150**, 423–447, doi:10.1007/s10546-013-9885-z.

——, and ——, 2015: Interactions between downslope flows and a developing cold-air pool. *Bound.-Layer Meteor.*, **154**, 57–80, doi:10.1007/s10546-014-9958-7.

Catalano, F., and A. Cenedese, 2010: High-resolution numerical modeling of thermally driven slope winds in a valley with strong capping. *J. Appl. Meteor. Climatol.*, **49**, 1859–1880, doi:10.1175/2010JAMC2385.1.

Chemel, C., and P. Burns, 2015: Pollutant dispersion in a developing valley cold-air pool. *Bound.-Layer Meteor.*, **154**, 391–408, doi:10.1007/s10546-014-9984-5.

Chen, F., and J. Dudhia, 2001: Coupling an advanced land-surface/hydrology model with the Penn State/NCAR MM5 modeling system. Part I: Model implementation and sensitivity. *Mon. Wea. Rev.*, **129**, 569–585, doi:10.1175/1520-0493(2001)129<0569:CAALSH>2.0.CO;2.

Deardorff, J. W., 1980: Stratocumulus-capped mixed layers derived from a three-dimensional model. *Bound.-Layer Meteor.*, **18**, 495–517, doi:10.1007/BF00119502.

Dudhia, J., 1989: Numerical study of convection observed during the winter monsoon experiment using a mesoscale two-dimensional model. *J. Atmos. Sci.*, **46**, 3077–3107, doi:10.1175/1520-0469(1989)046<3077:NSOCOD>2.0.CO;2.

Fast, J. D., S. Zhong, and C. D. Whiteman, 1996: Boundary layer evolution within a canyonland basin. Part II: Numerical simulations of nocturnal flows and heat budgets. *J. Appl. Meteor.*, **35**, 2162–2178, doi:10.1175/1520-0450(1996)035<2162:BLEWAC>2.0.CO;2.

Jiménez, P., J. Dudhia, J. F. González-Rouco, J. Navarro, J. P. Montávez, and E. García-Bustamante, 2012: A revised scheme for the WRF surface layer formulation. *Mon. Wea. Rev.*, **140**, 898–918, doi:10.1175/MWR-D-11-00056.1.

Katurji, M., and S. Zhong, 2012: The influence of topography and ambient stability on the characteristic of cold-air pools: A numerical investigation. *J. Appl. Meteor. Climatol.*, **51**, 1740–1749, doi:10.1175/JAMC-D-11-0169.1.

Kiefer, M. T., and S. Zhong, 2011: An idealized modeling study of nocturnal cooling processes inside a small enclosed basin. *J. Geophys. Res.*, **116**, D20127, doi:10.1029/2011JD016119.

Lee, T., I. Fukumori, and B. Tang, 2004: Temperature advection: Internal versus external processes. *J. Phys. Oceanogr.*, **34**, 1936–1944, doi:10.1175/1520-0485(2004)034<1936:TAIVEP>2.0.CO;2.

Lundquist, J., N. Pepin, and C. Rochford, 2008: Automated algorithm for mapping regions of cold-air pooling in complex terrain. *J. Geophys. Res.*, **113**, D22107, doi:10.1029/2008JD009879.

McKee, T. B., and R. D. O'Neal, 1989: The role of valley geometry and energy budget in the formation of nocturnal valley winds. *J. Appl. Meteor.*, **28**, 445–456, doi:10.1175/1520-0450(1989)028<0445:TROVGA>2.0.CO;2.

Mlawer, E. J., S. J. Taubman, P. D. Brown, M. J. Iacono, and S. A. Clough, 1997: Radiative transfer for inhomogeneous atmospheres: RRTM, a validated correlated-k model for the longwave. *J. Geophys. Res.*, **102**, 16 663–16 682, doi:10.1029/97JD00237.

Moeng, C. H., J. Dudhia, J. Klemp, and P. Sullivan, 2007: Examining two-way grid nesting for large eddy simulation of the PBL using the WRF model. *Mon. Wea. Rev.*, **135**, 2295–2311, doi:10.1175/MWR3406.1.

Muller, H., and C. D. Whiteman, 1988: Breakup of a nocturnal temperature inversion in the Dischma Valley during DISKUS. *J. Appl. Meteor.*, **27**, 188–194, doi:10.1175/1520-0450(1988)027<0188:BOANTI>2.0.CO;2.

Rampanelli, G., D. Zardi, and R. Rotunno, 2004: Mechanism of up-valley winds. *J. Atmos. Sci.*, **61**, 3097–3111, doi:10.1175/JAS-3354.1.

Rotach, M. W., G. Wohlfahrt, A. Hansel, M. Reif, J. Wagner, and A. Gohm, 2014: The world is not flat: Implications for the global carbon balance. *Bull. Amer. Meteor. Soc.*, **95**, 1021–1028, doi:10.1175/BAMS-D-13-00109.1.

Sakiyama, S. K., 1990: Drainage flow characteristics and inversion breakup in two Alberta mountain valleys. *J. Appl. Meteor.*, **29**, 1015–1030, doi:10.1175/1520-0450(1990)029<1015:DFCAIB>2.0.CO;2.

Schmidli, J., 2013: Daytime heat transfer processes over mountainous terrain. *J. Atmos. Sci.*, **70**, 4041–4066, doi:10.1175/JAS-D-13-083.1.

——, and R. Rotunno, 2010: Mechanism of along-valley winds and heat exchange over mountainous terrain. *J. Atmos. Sci.*, **67**, 3033–3047, doi:10.1175/2010JAS3473.1.

Skamarock, W. C., and Coauthors, 2008: A description of the Advanced Research WRF version 3. NCAR Tech. Note NCAR/TN-475+STR, 113 pp., doi:10.5065/D68S4MVH.

Vergeiner, I., and E. Dreiseitl, 1987: Valley winds and slope winds—Observations and elementary thoughts. *Meteor. Atmos. Phys.*, **36**, 264–286, doi:10.1007/BF01045154.

Wagner, A., 1938: Theorie und beobachtung der periodischen Gebirgswinde. *Gerlands Beitr. Geophys.*, **52**, 408–449.

Wagner, J. S., A. Gohm, and M. W. Rotach, 2015a: The impact of valley geometry on daytime thermally driven flows and vertical transport processes. *Quart. J. Roy. Meteor. Soc.*, **141**, 1780–1794, doi:10.1002/qj.2481.

——, ——, and ——, 2015b: Influence of along-valley terrain heterogeneity on exchange processes over idealized valleys. *Atmos. Chem. Phys.*, **15**, 6589–6603, doi:10.5194/acp-15-6589-2015.

Whiteman, C. D., 1990: Observations of thermally developed wind systems in mountainous terrain. *Atmospheric Processes over Complex Terrain*, *Meteor. Monogr.*, No. 45, Amer. Meteor. Soc., 5–42.

——, and S. Zhong, 2008: Downslope flows on a low-angle slope and their interactions with valley inversion. Part I: Observations. *J. Appl. Meteor. Climatol.*, **47**, 2023–2038, doi:10.1175/2007JAMC1669.1.

——, T. B. McKee, and J. C. Doran, 1996: Boundary layer evolution within a Canyonland basin. Part I: Mass, heat, and moisture budgets from observations. *J. Appl. Meteor.*, **35**, 2145–2161, doi:10.1175/1520-0450(1996)035<2145:BLEWAC>2.0.CO;2.

——, X. Bian, and J. L. Sutherland, 1999: Wintertime surface wind patterns in the Colorado River valley. *J. Appl. Meteor.*, **38**, 1118–1130, doi:10.1175/1520-0450(1999)038<1118:WSWPIT>2.0.CO;2.

Wicker, L. J., and W. C. Skamarock, 2002: Time-splitting methods for elastic models using forward time scheme. *Mon. Wea. Rev.*, **130**, 2088–2097, doi:10.1175/1520-0493(2002)130<2088:TSMFEM>2.0.CO;2.

Zardi, D., and C. D. Whiteman, 2013: Diurnal mountain wind systems. *Mountain Weather Research and Forecasting: Recent Progress and Current Challenges*, F. K. Chow, S. F. J. De Wekker, and B. J. Snyder, Eds., Springer Atmospheric Sciences, Springer, 35–119.